Numerical study on the dynamic fracture behavior of 3D heterogeneous rocks using General Particle Dynamics

P.Yin[a] H.C.Ma[a] X.W.Liu[bc] J.Bi[bc] X.P.Zhou[ab] FilippoBerto[d]

https://doi.org/10.1016/j.tafmec.2018.04.005

Abstract

The General Particle Dynamics code (GPD) is developed to simulate initiation, propagation and coalescence of cracks in 3D brittle rock specimens subjected to dynamic loads. In GPD, fractures of particles are determined through a damage evolution law of brittle rock materials. An elasto-brittle damage model is employed to reflect the initiation and growth of cracks and the macro-failure of brittle rocks. Numerical examples, including pre-notched semi-circular bending and uniaxial compression testing, have been carried out to verify the applicability of GPD to simulate the dynamic failure of rocks. Results of pre-notched semi-circular bend test show that GPD is capable of realistically simulating the mechanical behavior of rock materials subjected to dynamic loads. Under dynamic uniaxial loadings, the dynamic increment factor increases with increasing strain rate. Failure modes of samples pass from tensile to mixed shear-tension mode with increasing the loading speed. The number of fractions of sample increases with increasing the loading speed. Moreover, the failure mode of samples pass from a typical splitting failure to a mixed mode failure with decreasing heterogeneity coefficient while the number of cracks and fractions increases with decreasing the heterogeneity coefficient. The numerical results obtained from GPD are in excellent agreement with experiments and other numerical methods.

- **Previous** article in issue
- **Next** article in issue

Keywords

Progressive failure
Dynamic uniaxial compressive strength
Initiation, propagation and coalescence of cracks
Brittle rocks
General Particle Dynamics code

1. Introduction

Rock is a kind of heterogeneous medium, which is composed of one or more minerals. Under external loadings, cracks initiate, propagate and coalesce, leading eventually to the final fracture. The test results, such as ultimate stress and strain and rupture mode, are only the macroscopic reflection after a cumulative damage. Better understanding of the dynamic responses of rocks could impact positively in many applications such as rock mechanics, underground engineering and earthquake assessment. It is essential and important to understand how microcracks nucleate, propagate and coalesce under dynamic loads in order to provide a better understanding of fracture process of rocks in actual rock engineering. Numerical methods can be used to analyze the failure mechanism of rock specimens from the two aspects of the microcrack development and the macro mechanical behaviors, thus they become the focus of researches in the field of geotechnical engineering. Advanced numerical modeling is a successful tool to solve several rock engineering problems [1]. The Extended Finite Element Method (XFEM) [2] is very commonly used. By incorporating proper improvements based on FEM, the XFEM can successfully simulate simple and arbitrary crack initiation and growth. However, for more complicated problems, such as branch-cracking or multicrack problems, definition of the enrichment functions may be very difficult. Moreover, without a contact algorithm, it is challenging for XFEM to consider cracking, slipping and separation along the flaw direction. FDEM is a general-purpose numerical approach which combines continuum mechanicsprinciples, such as theory of elasticity and non-linear fracture mechanics, with discrete element algorithms to simulate multiple interacting, deformable, and fracturable solids [3]. However it lacks the ability of modelling heterogeneous and bedded rock samples. The Phase Field Method can be applied to simulate mixed mode crack propagation [4]. The fundamental concept behind this method is the introduction of a scalar phase field, which varies between 0 and 1, to represent the degree of fracture or damage of the material. However these phase-field models assume that the critical energy release rates for different crack modes are the same, which in fact is not the case for many materials. In rock-like materials, for example, the critical energy release rate for mode I fracture is significantly lower than that for mode II fracture.

The numerical manifold method (NMM) [5] can be applied to study initiation and propagation of cracks. It is a combination of the FEM and the discontinuous deformation analysis (DDA) [6]. The NMM is adopted to solve discontinuous problems involving stationary crack and crack propagation problems [7]. However, the crack tips are constrained to stop at the edges of the element, which reduces the accuracy if a crack tip happens to stop inside the element. In order to improve the accuracy,

singular physical covers containing the crack tips are enriched with the asymptotic crack-tip functions, then the stress intensity factors (SIFs) can be evaluated with a regular and relatively coarse mathematical cover system [8].

Meshless particle method can completely or partially eliminate the finite element grid, which is the base of the numerical methods as finite element methods, and displays unique advantages in the numerical simulation of large deformation, dynamic fracture, impact loadand fissile materials. It is worth mentioning here that Silling [9], [10], [11] proposed the bond-based peridynamic theory by precise deduction. In peridynamic theory, the non-local theory is applied to describe the internal effects between two limited distance particles in order to improve the calculation efficiency. The peridynamic theory has an advantage over both molecular dynamic methods and the classical finite element method. However, shear failureof rock cannot be very well simulated.

The Discrete Element Method [12] (DEM) has become popular as a meshfree method for analyzing the fracturing behavior of rocks. By simply breaking the bonds when the interaction force between two distinct elements overcomes the tensile or shear strength, the DEM can simulate the fracturing process of a rock without assuming where and how the cracks may be initiated [13], [14], [15], [16], [17], [18], [19]. Multiple attempts were made to simulate the fracturing behavior of rocks using the DEM [20], [21]. However, as mentioned in works by Donze et al. [22], the following limitations remain:

1. Size effect. The fracture roughness is found to depend on the radius of the discrete elements in a 2D analysis [21], which implies that the macroscopic fracturing behaviors of rocks predicted by the DEM are element dependent.
2. The cross effect. The element size and shape are different from those of real grains, which results in a cross-effect with the local constitutive laws of macroscopic behavior.
3. The local/macroscopic constitutive laws. Although complicated constitutive laws are not required for the DEM, the relationships between the local and macroscopic constitutive laws are needed. However, the establishment of these relationships by only using data which are obtained from classical geomechanical tests is impractical when attempting to obtain a desirable single solution set.

Smoothed particle hydrodynamics (SPH) [23], [24], [25], [26], [27], [28], [29], [30], [31] is one of the earliest meshfree Lagrangian particle methods. In SPH, an interaction

between any two particles is only controlled by the kernel function and the interaction is automatically terminated if one leaves the influence domain of the other. This inherent crack treatment by defining influence only within the interaction domain of the basis function [32], [33], is ill-equipped to simulate initiation and propagation and coalescence of the flaws.

In this paper, the General Particle Dynamics code [34], [35], [36], [37], which is based on SPH and overcomes some disadvantages of SPH, is developed and employed to simulate the initiation, propagation and coalescence of cracks in rocks at different loading rate. Ability of the proposed numerical method to accurately assess the initiation and the propagation and coalescence of cracks is demonstrated by few examples [38].

2. The damage model of General Particle Dynamics (GPD)

In this paper, only the damage model implemented in the GPD is described in detail because the general formulations of the methods such as constitutive model, governing equations, correction for consistency have been just widely discussed in previous contributions [34], [35], [36], [37].

2.1. Particle distribution in the numerical models

When a heterogeneous rock material is involved, the disorder of microstructures in rock mass should be simulated by means of numerical models. To simulate the random microstructures in rocks, rock heterogeneity can be well characterized by using statistical approaches. Disorder is defined by randomly distributing the mechanical properties of particles. The statistical distribution of mechanical parameters of particles can be described by the Weibull distribution function [39]. These mechanical parameters of particles include the uniaxial compression strength, Young's modulus, Poisson ratio and unit weight. In this study, only uniaxial compression strength of particles is described by using the Weibull distribution theory.

The Weibull distribution function is expressed as follows in agreement with Ref. [39]:

(1)W(x)=ωλ0λλ0ω-1exp-λλ0ω

where *x* denotes the mechanical parameter of particles which is described by the Weibull distribution function, ω defines the shape of the Weibull distribution function, and can be referred to as the homogeneity index, λ is the mechanical parameter of one particle, and λ0(Young's modulus) is the mean value of the parameter of all the particles. According to the Weibull distribution [39], a larger ω value indicates that more

particles have the mechanical properties which are approximated to the mean value, which describes among homogeneous rock samples, as shown in Fig. 1.

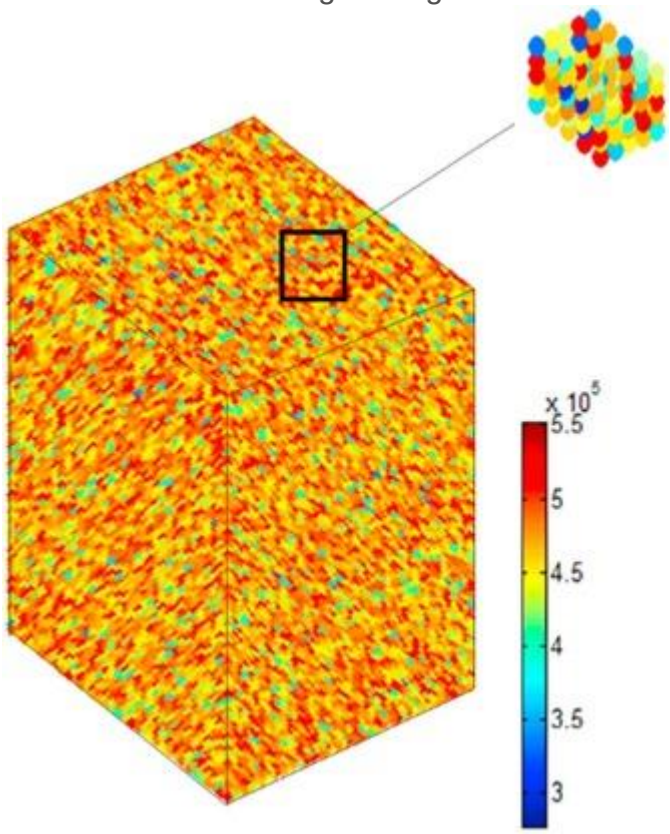

1. Download high-res image (191KB)
2. Download full-size image

Fig. 1. The uniaxial compressive strength distribution of 3D particles in the numerical model (Pa).

2.2. Damage in particles

In most cases, rocks fail in a brittle manner. All the particles have the same parameters as that of the parent material (i.e. uniaxial compressive strength, Young's modulus (E) and Poisson ratio (v), etc.), therefore the damage initiation and growth in particles are determined by the damage model of parent materials. The failure criterion is described as follows:

In this paper, the 3D Hoek-Brown Strength (failure) criterion [40], which is developed based on the 2D Hoek-Brown Strength (failure) and Mogi Strength (failure) criteria, is applied to determine the damage initiation. A damage is thought to be initiated from one particle when the tensile stress or tangential stress between the neighboring particles satisfies the 3D Hoek-Brown strength (failure) criterion [40].

Based on the true triaxial compression test data on rock and taking the effects of intermediate principal stress into account, the 3D Hoek-Brown strength (failure) criterion for rocks is proposed as follows [40]:

(2)92σcτoct2+322miτoct-miσm,2=sσc

(3)τoct=13(σ1-σ2)2+(σ2-σ3)2+(σ3-σ1)2

where σc is an uniaxial compressive strength of an intact rock, σm,2 is average of the maximum and minimum principal stress, τoct is the octahedral shear stress, *m* and *s* are the material parameter as same as those in the Hoek–Brown criterion, which are defined by Hoek et al. and take the following form [41], [42], [43], [44]:

(4)m=miexpGSI-10028-14D0

(5)s=miexpGSI-1009-3D0

where D_0 is a disturbance coefficient which varies from 0.0 for the undisturbed in situ rock masses to 1.0 for very disturbed rock masses [41], [42], [43], [44], m_i is the value of *m* for intact rock and can be obtained by experiments. The parameter m_i varies from 4 for very fine weak rock like claystone to 33 for coarse igneous light-colored rock like granite. In this paper m = 25 and s = 0.86 have been employed. *m* and *s* are calculated based on complete laboratory test block with RMR = 100 and Q = 500. The 3D H-B strength criterion considers the difference of tensile and compressive strengths of rocks, the effects of intermediate principal stress on rock strength, fracturing degree of rock mass, and the behavior of failure envelope with a parabola formula. Therefore, the 3D H-B strength criterion has extensive applicability in rock and rock material.

Now we introduce a parameter *f*, named as the 'interaction factor' which defines the level of interaction between the *i*-th and the *j*-th particles. This interaction factor *f* is determined based on the real damage in material particles. Initially, for undamaged particles, f=1, which implies 'full interaction'. With progressing of damage, *f* finally becomes zero for fully damaged particle. In order to model the damage growth, a linear elastic brittle law is used, as shown in Fig. 2.

(6)Df=0,andf=1,(ifσi<σmax)

(7)Df=1,andf=0,(ifparticledamaged)

where Df is the damage factor, and *f* is the interaction factor.

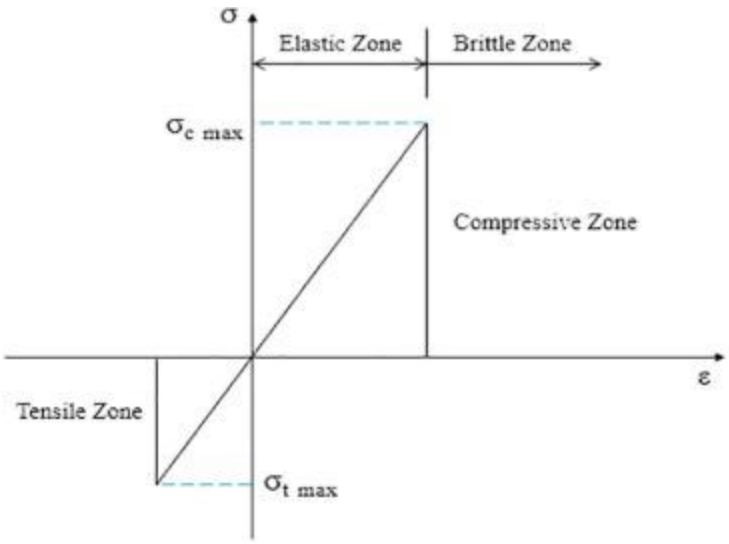

1. Download high-res image (25KB)
2. Download full-size image

Fig. 2. Linear elastic brittle law.

Once the damage is initiated from one particle, their interactions are no longer the same as those in the undamaged material. Although the damaged particles do not disappear and are still in the influence domain of others, the damaged particle is traction free and the damaged particle has no influence on the surrounding particles in the stress calculation because the interaction factor *f* is 0. For the damaged particles, since its stresses become zero, the surrounding living particles have no influence on them. A new boundary is formed, as shown in Fig. 3.

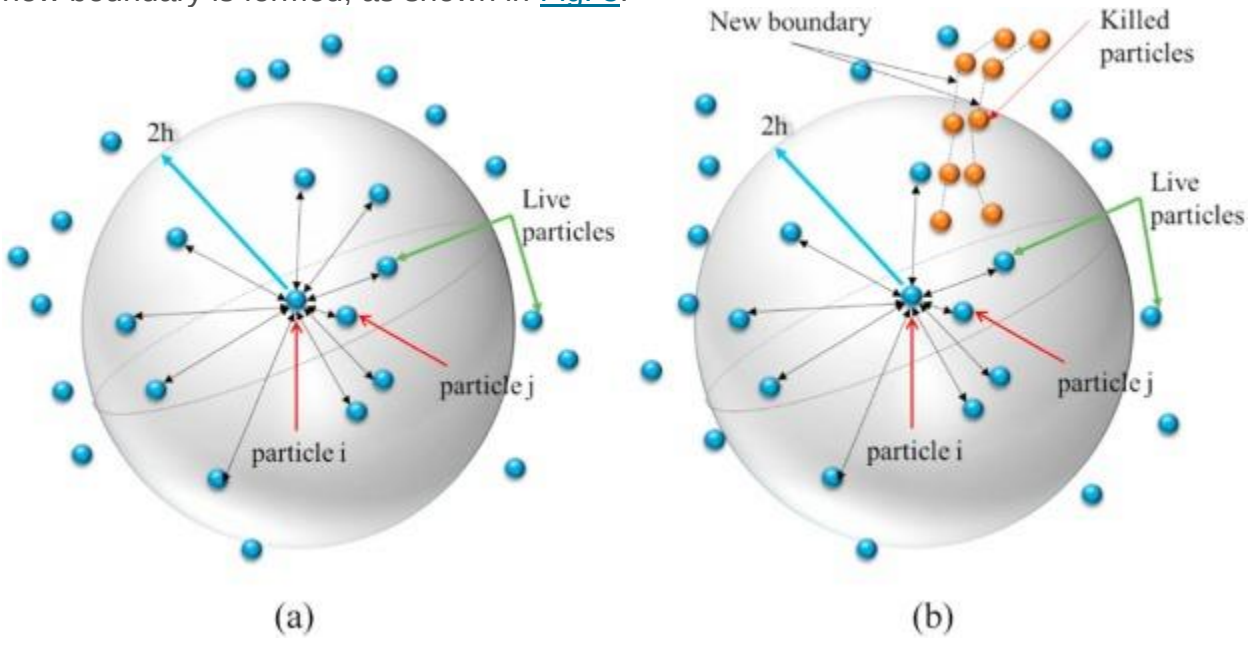

1. Download high-res image (100KB)

2. Download full-size image

Fig. 3. 3D particle discretization: (a) undamaged configuration, (b) cracked configuration.

3. Numerical simulation

3.1. A benchmark example

In order to validate the numerical model in the initiation and propagation of cracks, the behavior of pre-notched semi-circular bend (NSCB) under impact load is investigated firstly.

The numerical simulation performed in this paper is based on the laboratory results by Zhang and Zhao [45]. The rock used is Fangshan Marble sourced in the Fangshan area in Beijing, China. One laboratory test of NSCB was performed. The specimen size for NSCB is plotted in Fig. 4(a). It has a diameter of 50 mm, with a notch length of 5 mm and a span length of 33.3 mm. To reproduce the laboratory tests, NSCB numerical model for GPD is created, as shown in Fig. 4(b).

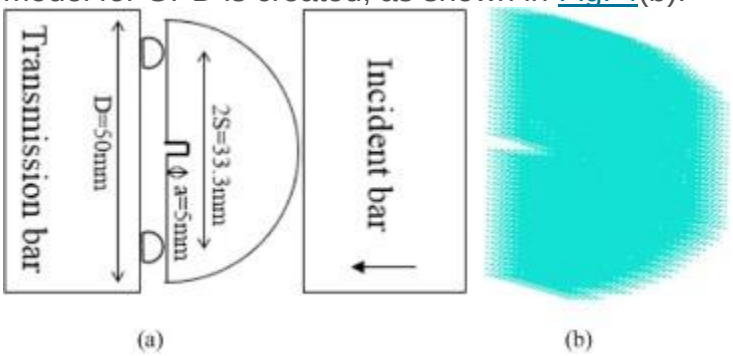

1. Download high-res image (47KB)
2. Download full-size image

Fig. 4. Schematic diagram of NSCB sample: (a) laboratory test; (b) GPD model.

The material parameters for numerical simulation including the Young's modulus (E), Poisson's ratio (υ), Density (ρ), Uniaxial compressive strength (σ_c), strength parameters m and s are listed in Table 1. The other computational data are also provided in Table 1.

Table 1. Computational parameter of Fangshan marble for the numerical simulation.

Calculation parameters	
$\rho = 2650\ kg/m^3$	m = 25 (Hoek-Brown strength criterion)
E = 32 GPa	s = 0.86 (Hoek-Brown strength criterion)
$v = 0.21$	$\Delta t = 1\ \mu s$ (time step of GPD)

Calculation parameters
$\sigma_c = 200$ MPa

In the NSCB laboratory test using SHPB, a striking velocity of about 2.25 m/s is applied on the incident bar through a striker. Therefore, in the numerical simulation, the same impact speed of the incident bar is applied.

During numerical simulation process, the overall direction of crack propagation is parallel to the loading direction. The crack-tip initiates from the end of the pre-notched crack and propagates towards the right end of the model, as shown in Fig. 5. The numerical results obtained from UDEC are plotted in Fig. 5(a). A small local fracture zone obtained from GPD starts at 45 μs due to the local high strain rate, as shown in Fig. 5(b). Then, the experimental results are depicted in Fig. 5(c). At the end of the loading period, the model is splitted into two halves by the final crack, as shown in Fig. 5. The numerical results by GPD are in sound agreement with those by UDEC and experiment, as shown in Fig. 5.

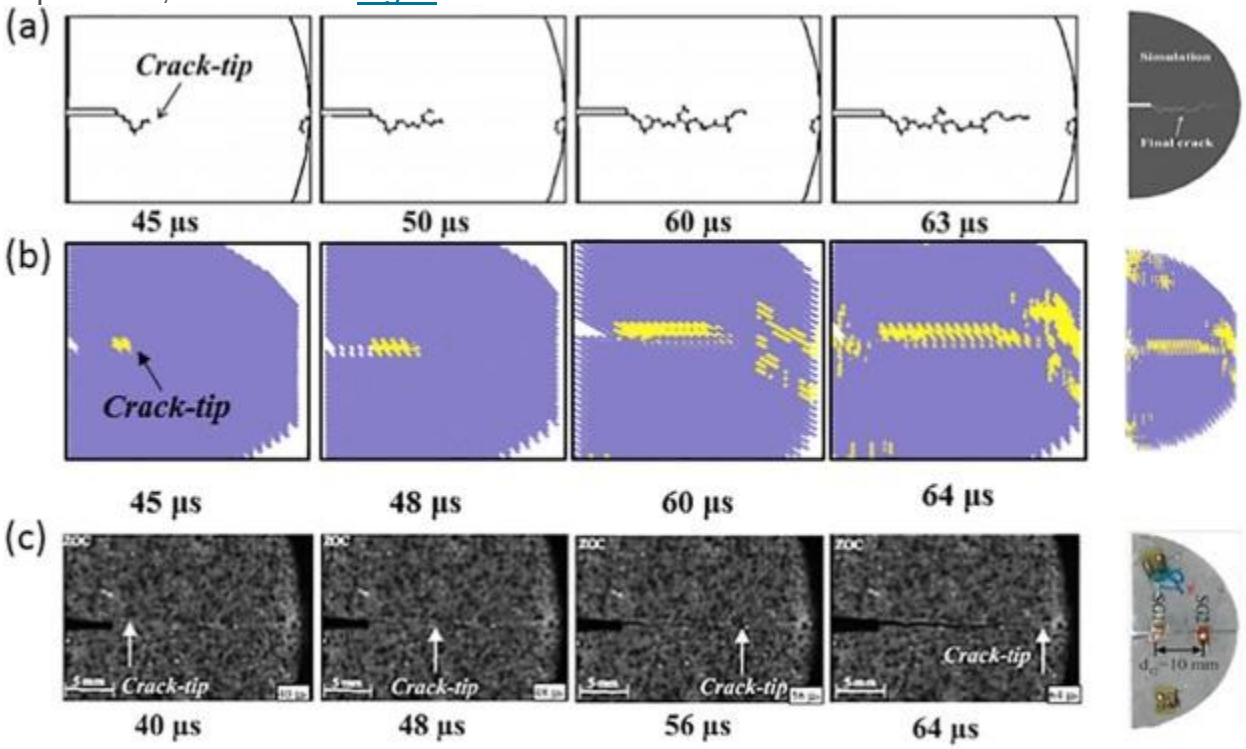

1. Download high-res image (167KB)
2. Download full-size image

Fig. 5. Comparison of crack-tip propagation process and final crack pattern at 200 μs: (a) UDEC results [45], (b) GPD results, (c) experimental results [45].

In order to quantify the reliability of the proposed numerical approach, the crack speed and crack-tip position in GPD are compared with those observed in UDEC software and experiment. The crack propagation speed is calculated based on the distance between two consecutive crack tip positions and the time required to propagate between the two positions. As shown in Fig. 6, the variables of crack-tip position and crack propagation speed are in good agreement with the UDEC and experimental results. The crack-tip propagation speed in GPD is slightly slower than that in the experiment, and almost the same as that in UDEC. The crack propagation speed in simulation of GPD is 600 m/s at 45 μs, then it increases to 660 m/s at 48 μs. At 60 μs, the crack speed reaches the peak of 750 m/s, and finally drops to 500 m/s. It is slightly faster than that in UDEC and experiments. This implies that crack propagation speed in simulation first increases, and then decreases.

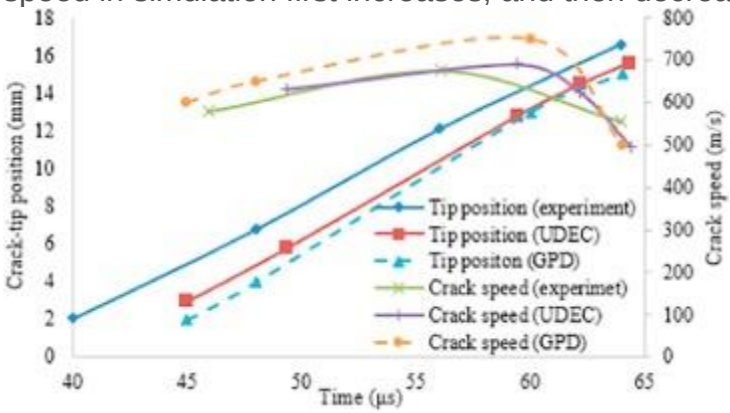

1. Download high-res image (59KB)
2. Download full-size image

Fig. 6. Comparison of crack-tip position and cracking speed between the experiment and the numerical simulation.

To quantify the reliability of the proposed numerical approach, the impact loads on incident bar evolving with time in GPD and experiment are plotted in Fig. 7. The increase of impact force on incident bar in GPD is slightly slower than that of experiment. While, the peak value of impact force in GPD is minor higher than that in experiment. As shown in Fig. 7, the impact force on incident bar in GPD is in good agreement with the experimental results.

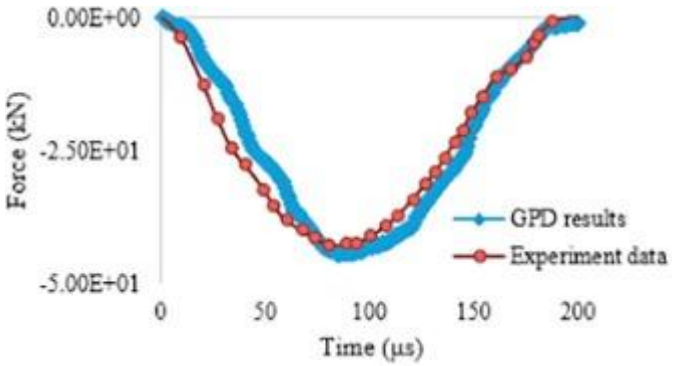

1. Download high-res image (32KB)
2. Download full-size image

Fig. 7. Dynamic force on incident bar.

3.2. The effect of heterogeneity coefficient on the failure mode of sample under dynamic uniaxial compression

For the dynamic uniaxial compression test, the simplified loading diagram on the x-y plane is plotted in Fig. 8.

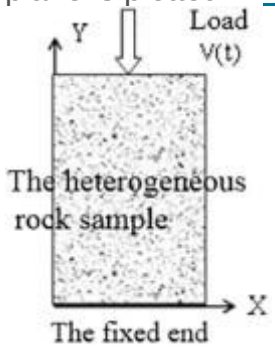

1. Download high-res image (37KB)
2. Download full-size image

Fig. 8. Schematic diagram of X-Y plane under dynamic uniaxial compressive loads.

In samples subjected to dynamic uniaxial compression loads, particles represent the geometry of 60 mm (length) × 50 mm (width) × 20 mm (thickness) in scale, as shown in Fig. 9. Material properties and other computational data are given in Table 2. The solid wallboundary is free slip boundary condition in this paper.

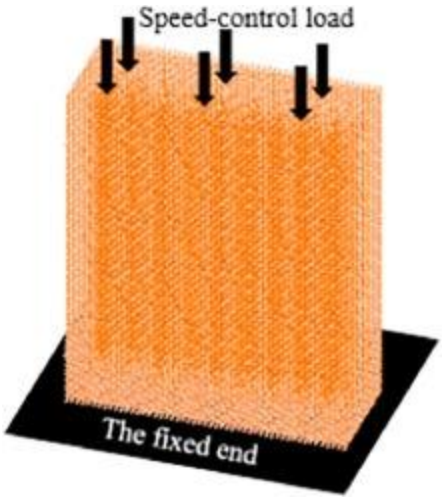

1. Download high-res image (91KB)
2. Download full-size image

Fig. 9. GPD model.

Table 2. Computational parameter for the numerical simulation in the dynamic unaxial compression test.

Calculation parameters	
$\rho = 2650\ kg/m^3$	m = 25 (Hoek-Brown strength criterion)
E = 32 GPa	s = 0.86 (Hoek-Brown strength criterion)
v = 0.21	$\Delta t = 1\ \mu s$ (time step of GPD)

In this subsection, the effect of heterogeneity coefficient with different values ($w = 5$, 10 and 20) on the failure mode of samples subjected to dynamic uniaxial compression is studied. The strain rate is $\dot{\varepsilon}=\frac{Loading velocity}{Sample height}=\frac{0.06}{=33.33s-1}$. It belongs to the medium strain rate regime.

As shown in Fig. 10, the numerical results of sample 1 are plotted for the heterogeneity coefficient $w = 20$. When the loading reaches step 1000, wing cracks ①, ② and ③ are initiated from the middle of sample 1. When the loading reaches step 1150, wing cracks ①, ② and ③ propagate towards top and bottom edges of sample. When the loading reaches step 1550, out-of-plane shear crack I initiated from the lower tip of wing crack ② coalesces with wing crack ①. Meanwhile, out-of-plane shear crack II initiated from the tip of wing crack ③ coalesces wing crack ②. Then, the specimen is splitted into three fractions in the splitting failure mode.

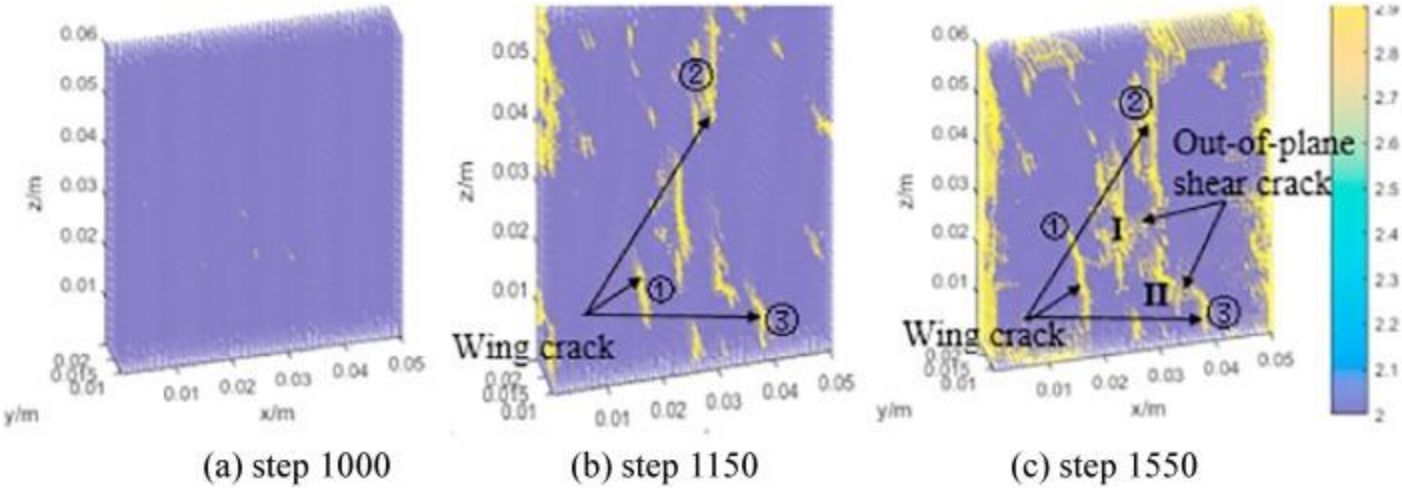

(a) step 1000 (b) step 1150 (c) step 1550

1. Download high-res image (263KB)
2. Download full-size image

Fig. 10. Crack initiation, propagation and coalescence in rectangular specimen at strain rate of 33.33s-1($w = 20$).

As shown in Fig. 11, the numerical results are plotted for the heterogeneity coefficient $w = 10$. This model is defined as sample 2. When the loading reaches step 600, wing cracks ①, ② and ③ are initiated from the middle of sample. When the loading reaches step 1000, wing cracks ①, ② and ③ grow towards the top and bottom edges of sample, oblique shear crack (1) is initiated near the tip of wing crack ② and propagates towards the bottom edge. When the loading reaches step 1750, oblique shear crack (1) coalesces with wing crack ② and wing crack ①, oblique shear crack (2) initiated near the tip of wing crack ③ coalesces with wing crack ②. The sample 2 is splitted into six fractions in the mixed shear-tension failure mode.

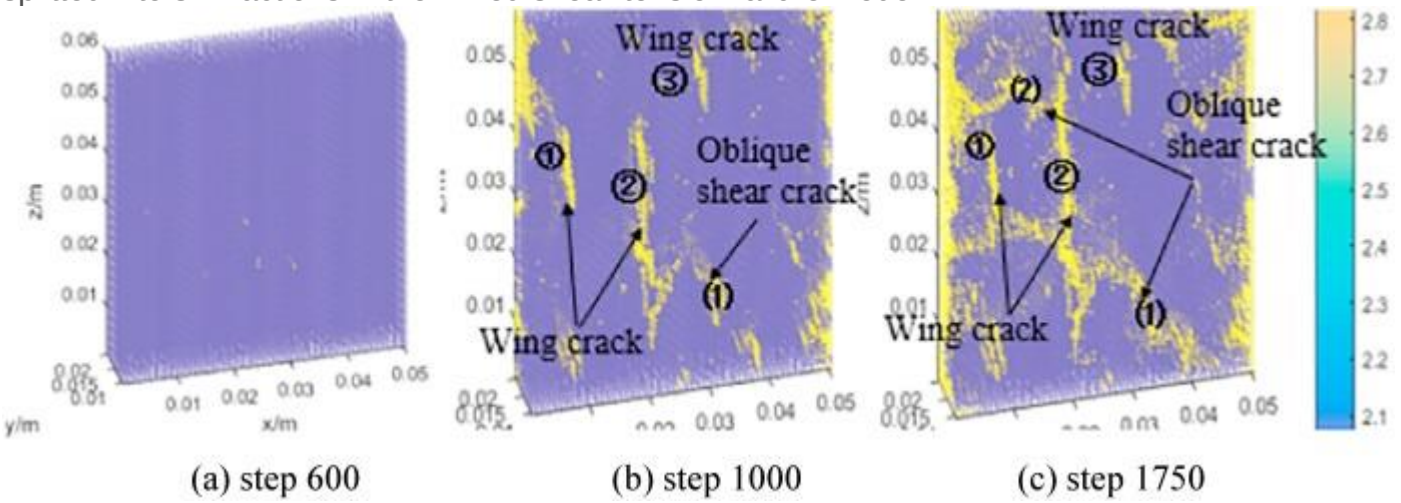

(a) step 600 (b) step 1000 (c) step 1750

1. Download high-res image (310KB)
2. Download full-size image

Fig. 11. Crack initiation, propagation and coalescence in rectangular specimen at strain rate of 33.33s-1($w = 10$).

Numerical results for heterogeneity coefficient $w = 5$ are plotted in Fig. 12. This sample is defined as sample 3. When the loading reaches step 400, much more damaged particles initiate from sample due to the more uneven particle strength. When the loading reaches step 700, a number of oblique shear cracks initiate from the upper and lower edges of sample, such as oblique shear crack (1) and oblique shear crack (2). When the loading reaches step 1050, oblique shear crack (3) initiates from the bottom of sample and propagates towards the right edge of sample, wing crack ① coalesces with oblique shear crack (2) and oblique shear crack (3). Then, the model is splitted into more than six fractions by the final cracks in the mixed shear and tension failure mode.

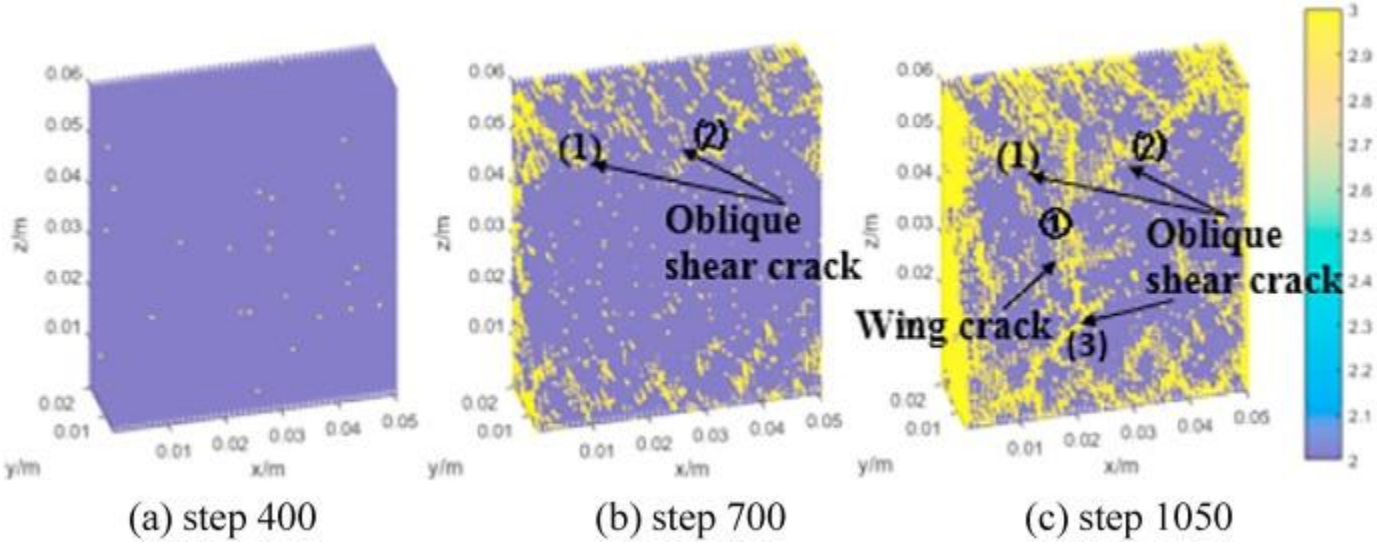

1. Download high-res image (313KB)
2. Download full-size image

Fig. 12. Crack initiation, propagation and coalescence in rectangular specimen at strain rate of 33.33s-1($w = 5$).

It is found from Fig. 10, Fig. 11, Fig. 12 that the failure mode of samples transform from splitting failure to the mixed shear-tension failure with decreasing heterogeneity coefficient. Moreover, the number of cracks and fractions increases with decreasing heterogeneity coefficient. The stress-strain curves at the different heterogeneity coefficient obtained from GPD are plotted in Fig. 13. The crack initiation stress decreases from 112.60 MPa in sample 1 to 61.2 MPa in sample 3. The peak stress of sample decreases from 123.58 MPa in sample 1 to 79.25 MPa in sample 3. The peak strain decreases from 0.357% in sample 1 to 0.271% in sample 3. That is to say, the crack initiating stress, peak stress and peak normal strain of sample decrease with

decreasing heterogeneity coefficient. Therefore, the heterogeneity coefficient has a significant influence on the sample strength, crack initiation stress and the failure mode, as shown in Fig. 13.

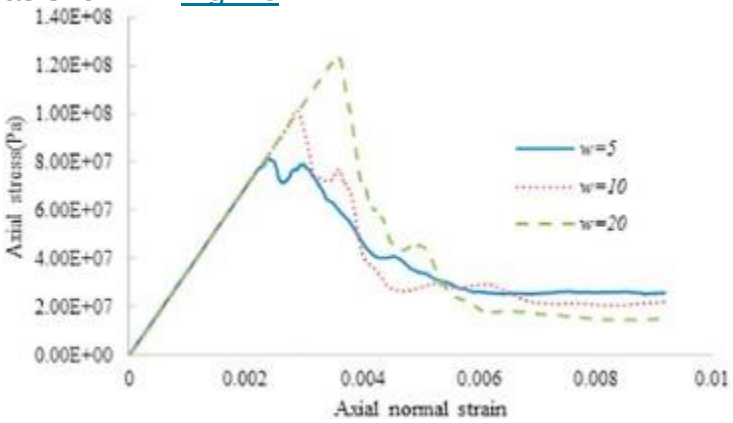

1. Download high-res image (38KB)
2. Download full-size image

Fig. 13. Stress-strain curves obtained from GPD at strain rate of 33.33s-1 at the different heterogeneity coefficient (w = 5, w = 10 and w = 20).

3.3. The effect of strain rate on the failure mode of sample under dynamic uniaxial compression

3.3.1. Low strain rate

3.3.1.1. The strain rate of 1s-1

In sample 4, velocity of the fixed boundary is 0, the loading velocity is 0.06 m/s. The strain rate is ε̇=LoadingvelocitySampleheight=0.060.06=1s-1. It belongs to the low strain rate regime. The heterogeneity coefficient is equal to 20. The calculation parameters are listed in Table 2.

The vertical stress contour evolving with time in sample 4 is plotted in Fig. 14. At step 24,000, some particles in the sample 4 are locally damaged under compressive stress of 78.26 MPa, which is corresponding to the red[1] point in stress-strain curve in Fig. 15. With the increase of compressive loads, more particles are damaged around the nucleation point of crack due to stress concentration. When the loading reaches step 26,750, the compressive stress reaches 86.75 MPa, the crack propagates towards the top of sample. When the compressive stress equals to 92.01 MPa, bearing capacity of the sample 4 reaches the maximum. After peak value, the bearing capacity of sample quickly reduces due to more and more damaged particles. Finally, crack coalescence appears, the failure of the sample 4 occurs. The stress-strain curve of sample 4 is plotted in Fig. 15. The red point represents initiation of crack, the green

point represents peak strength and the blue point is the crack coalescence. As expected, the stress-strain curve in Fig. 15 exhibits the elastic-brittle behaviors.

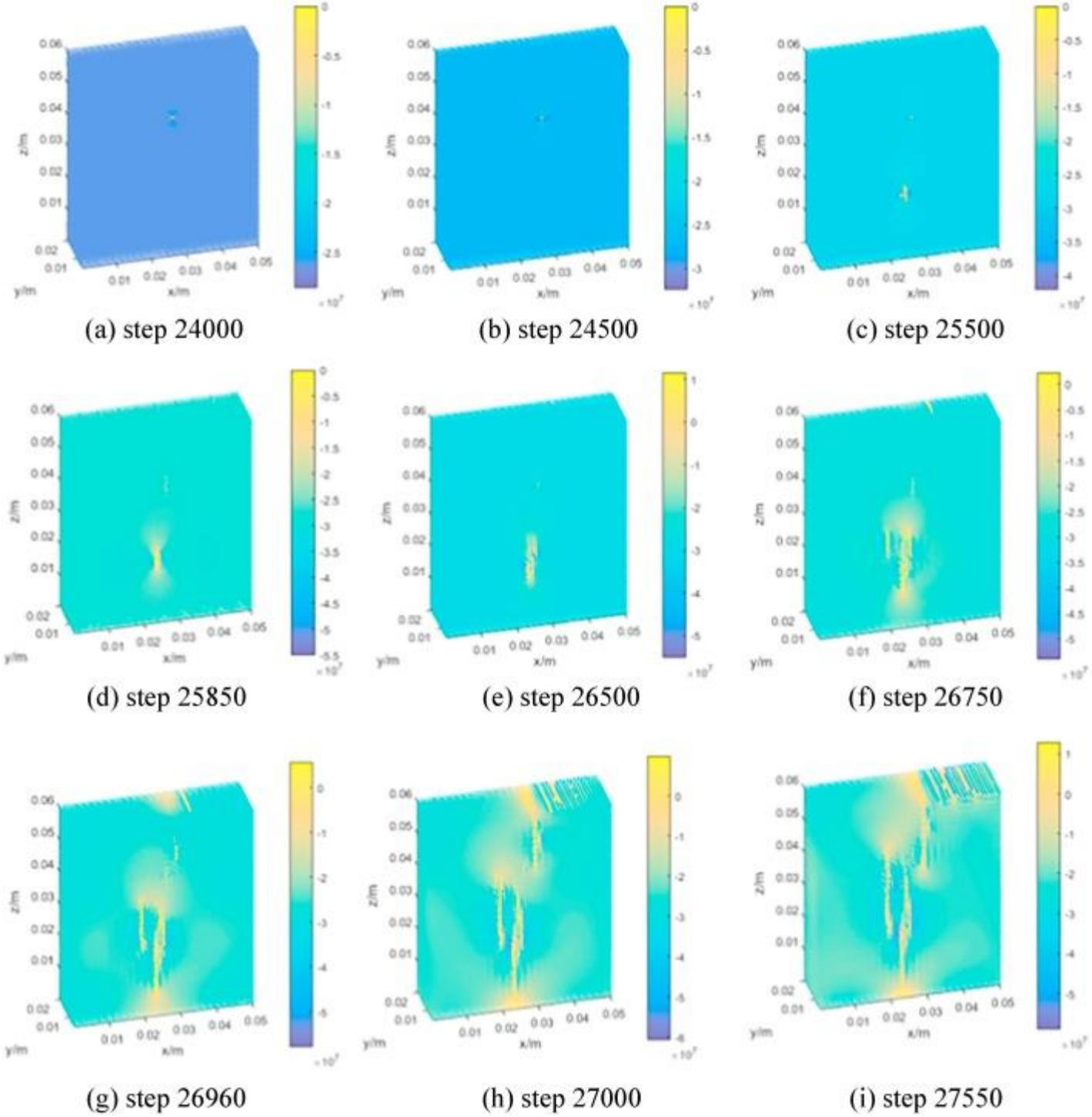

1. Download high-res image (517KB)
2. Download full-size image

Fig. 14. Vertical stress contour plot of the sample 4 at strain rate of 1 s^{-1}.

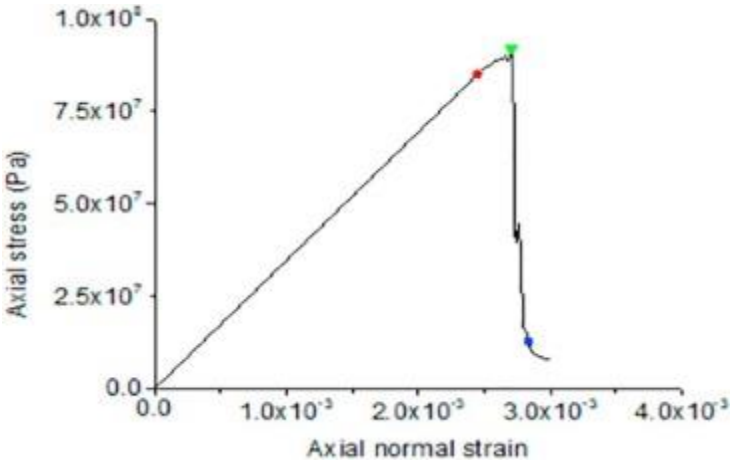

1. Download high-res image (37KB)
2. Download full-size image

Fig. 15. The numerical stress-strain curves of the sample 4 at strain rate of 1 s^{-1}.

In this sample, the damaged particles are plotted in red color to describe the initiation and propagation of cracks, as shown in Fig. 16. When the loading reaches step 24,000, a wing crack emanates from the upper of sample. When the loading reaches step 25,500, the other wing crack initiates from the bottom of sample and propagates towards the top and bottom edges of sample. With the increase of loading, wing cracks keep growing. When the loading reaches step 27,550, wing cracks coalesce with each other through an out-of-plane shear crack initiating from the lower wing crack, and the failure of the sample 4 occurs at the same time. The failure mode of cuboid rock sample under uniaxial compression at strain rate of1 s^{-1} is typical splitting failure, as shown in Fig. 17.

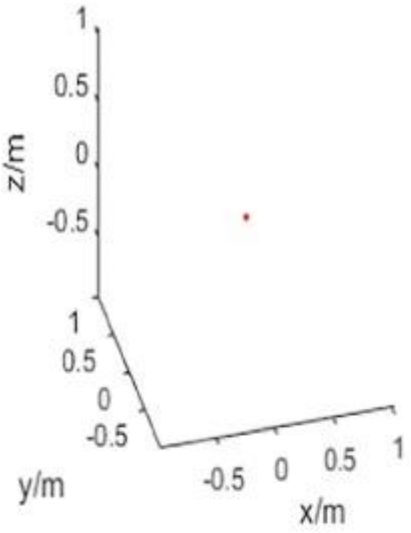

(a) step 24000

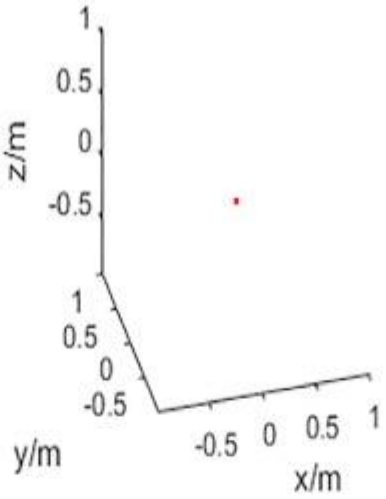

(b) step 24500

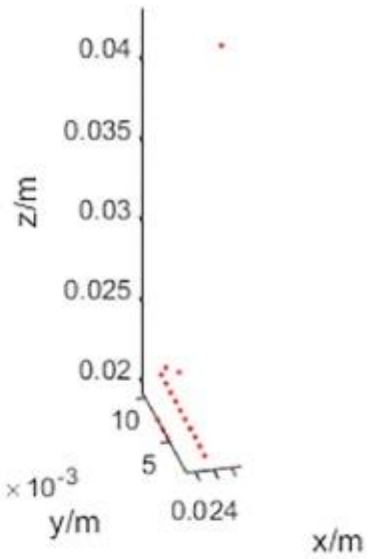

(c) step 25500

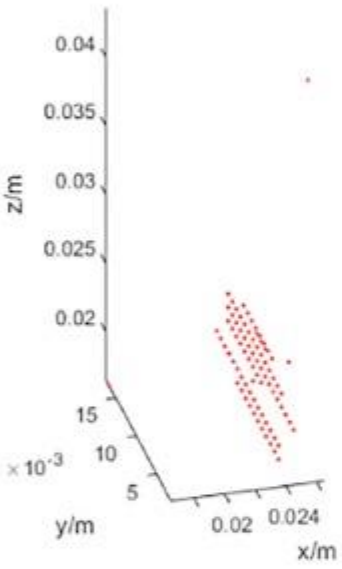

(d) step 25850

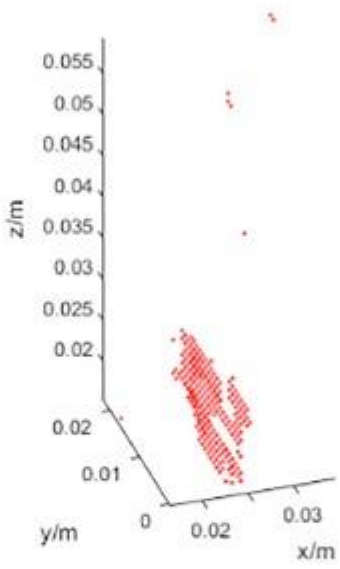

(e) step 26500

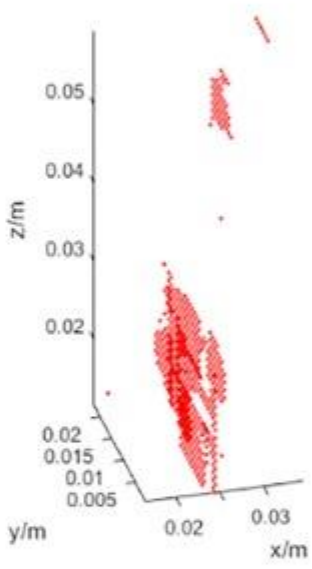

(f) step 26570

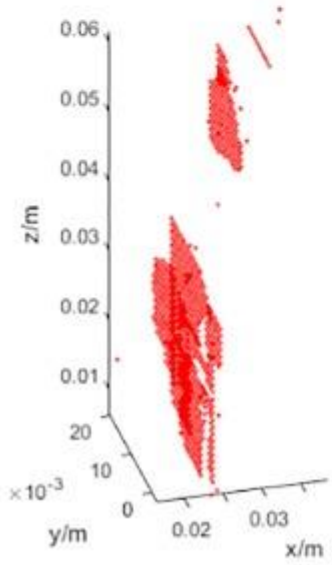

(g) step 26960

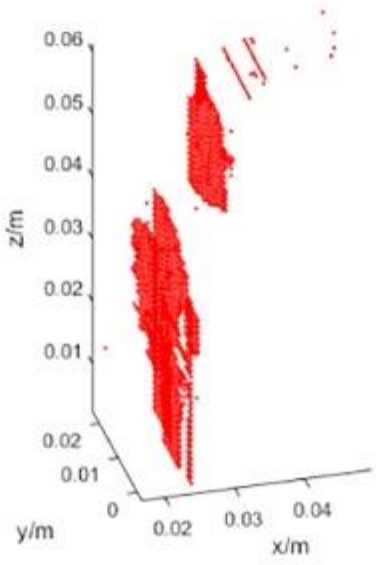

(h) step 27000

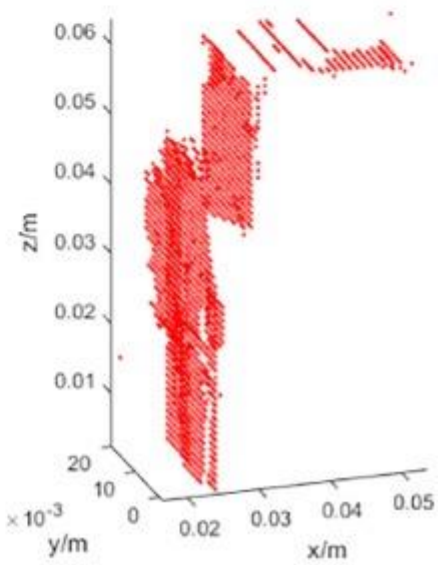

(i) step 27550

1. Download high-res image (515KB)
2. Download full-size image

Fig. 16. Space distribution of the damaged particles at strain rate of 1 s^{-1}.

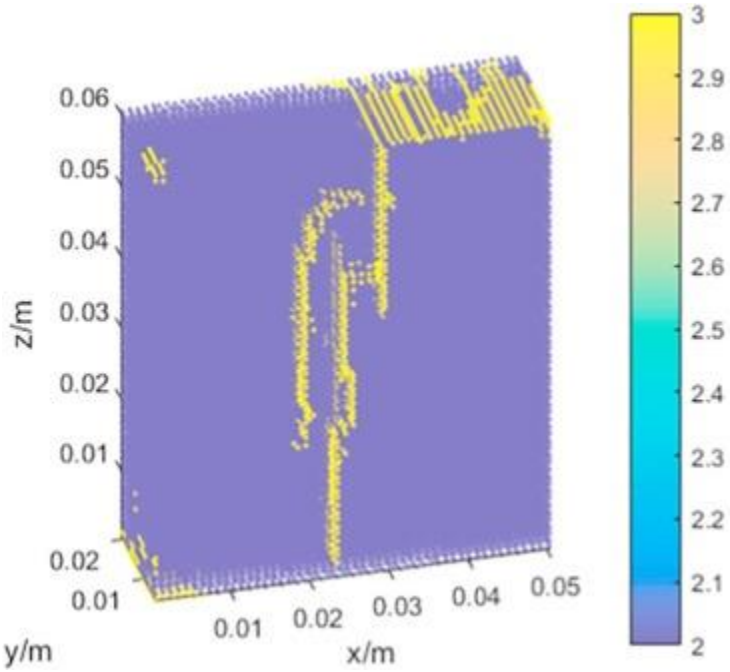

1. Download high-res image (61KB)
2. Download full-size image

Fig. 17. Failure mode of the sample 4 at strain rate of 1 s^{-1}.

3.3.2. Medium strain rate

3.3.2.1. The strain rate of 6.67 s^{-1}

This model is defined as the sample 5. The loading velocity is 0.4 m/s. The strain rate is $\dot{\varepsilon}$=LoadingvelocitySampleheight=0.40.06=6.67s-1. This level of strain belongs to the medium strain rate. The heterogeneity coefficient is equal to 20. The calculation parameters are listed in Table 2.

In GPD, the proposed strategy effectively captures the vertical stress contour to describe initiation and propagation of cracks in the sample 5 simulated by damaged particle at different step, as shown in Fig. 18.

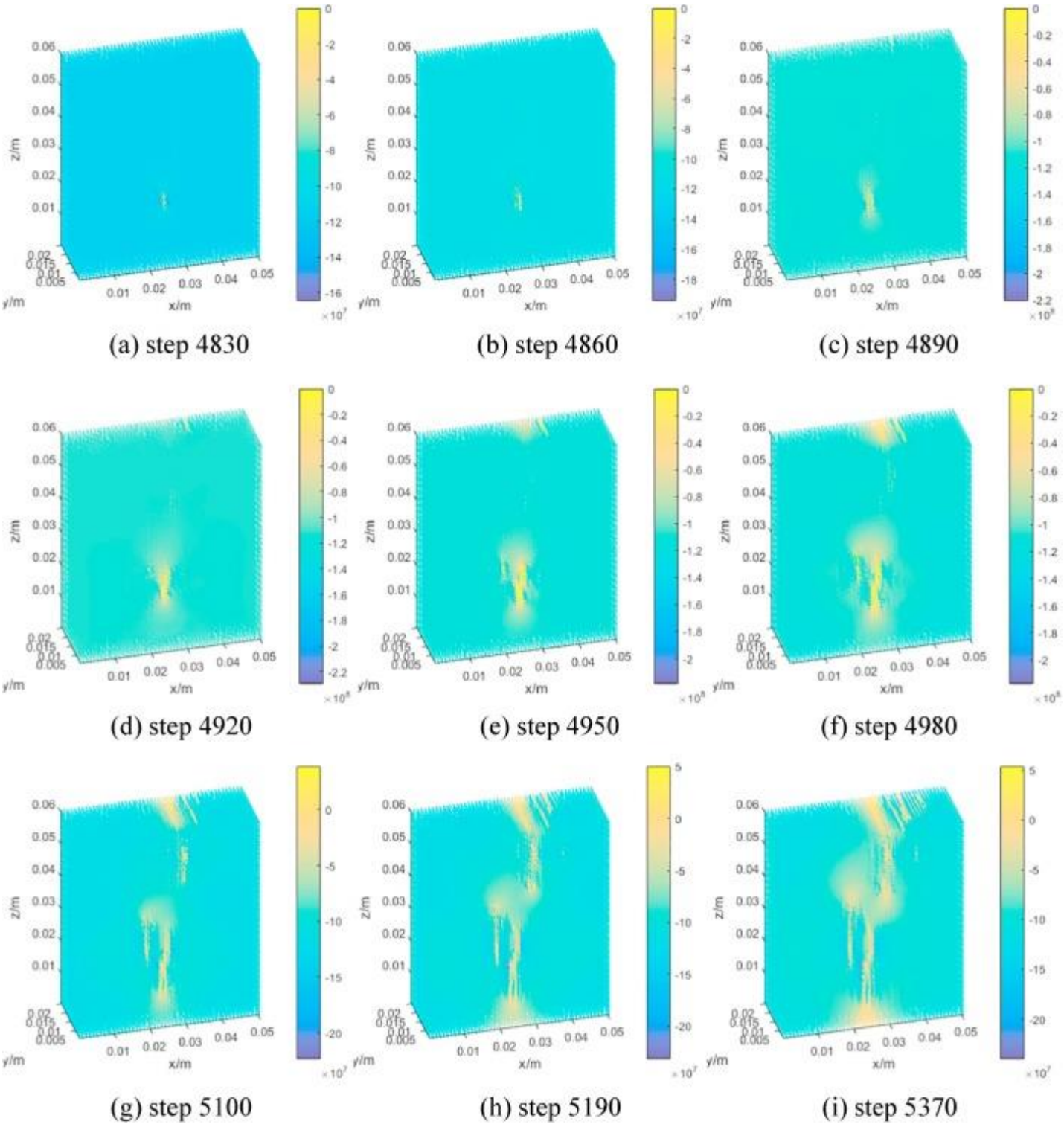

1. Download high-res image (761KB)
2. Download full-size image

Fig. 18. Vertical stress contour plot of the sample 5 at strain rate of 6.67 s^{-1}.

The vertical strain contour of the sample 5 is plotted in Fig. 18. At step 4830, some particles in the sample 5 are first locally damaged under compressive stress of 92.09 MPa corresponding to the red point in the stress-strain curve in Fig. 19. When the loading reaches step 5370, the compressive stress reaches 96.30 MPa, and the crack propagates towards the top of the sample 5. When the compressive stress is equal to 96.44 MPa, the compression stress reaches the peak value. After that, the bearing capacity of sample quickly reduces. Finally, crack coalescence appears, the splitting failure of the sample 5 occurs. The stress-strain curve of sample 5 is plotted in Fig. 19. The final failure of sample 5 is shown in Fig. 20.

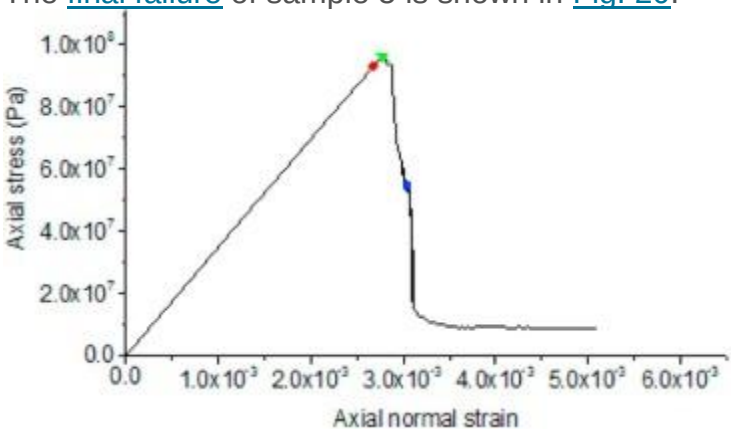

1. Download high-res image (42KB)
2. Download full-size image

Fig. 19. The numerical stress-strain curves of the sample 5 at strain rate of 6.67 s^{-1}.

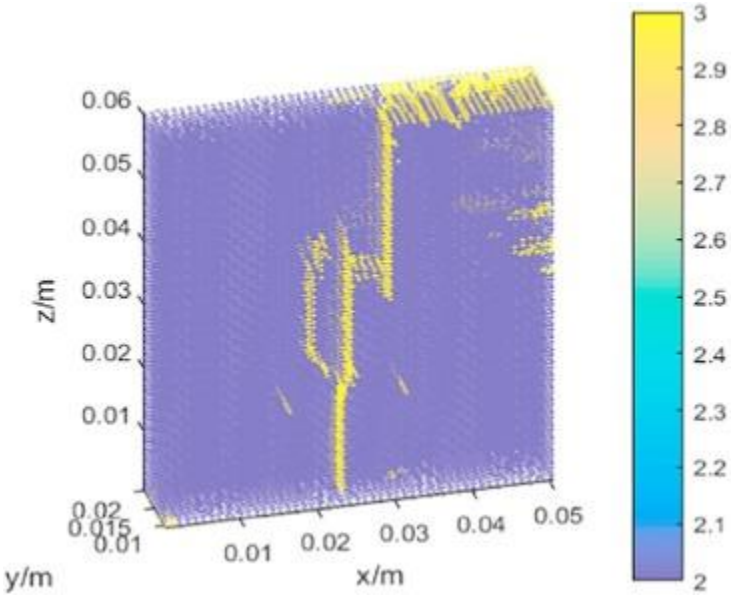

1. Download high-res image (76KB)
2. Download full-size image

Fig. 20. Failure mode of rock samples at strain rate of 6.67 s^{-1}.

3.3.2.2. The strain rate of 66.67s-1

In this subsection, the loading speed is 4 m/s. The strain rate is $\dot{\varepsilon}=\frac{Loading velocity}{Sample height}=\frac{4}{0.06}=66.67s-1$.

This medium strain rate belongs to medium regime. The heterogeneity coefficient is equal to 20. The calculation parameters are listed in Table 2.

This model is defined as the sample 6. The numerical results are plotted in Fig. 21. When the loading reaches step 500, wing cracks initiate from the middle of sample, as shown in Fig. 21(a). When the loading reaches step 550, wing cracks propagate along the direction of the maximum principal stress, as shown in Fig. 21(b). In Fig. 21(c), the loading reaches step 900. Oblique shear crack (1) initiated from the bottom edge coalesces with wing crack ②. Meanwhile, oblique shear crack (2) initiated from the top edge of sample coalesces with wing crack ②. Out-of-plane shear crack I emanating from the tip of wing crack ② coalesces with wing crack ①. Out-of-plane shear crack II emanating from the tip of wing crack ① coalesces with wing crack ③. Then, the sample 6 fails in the mixed shear-tension failure mode.

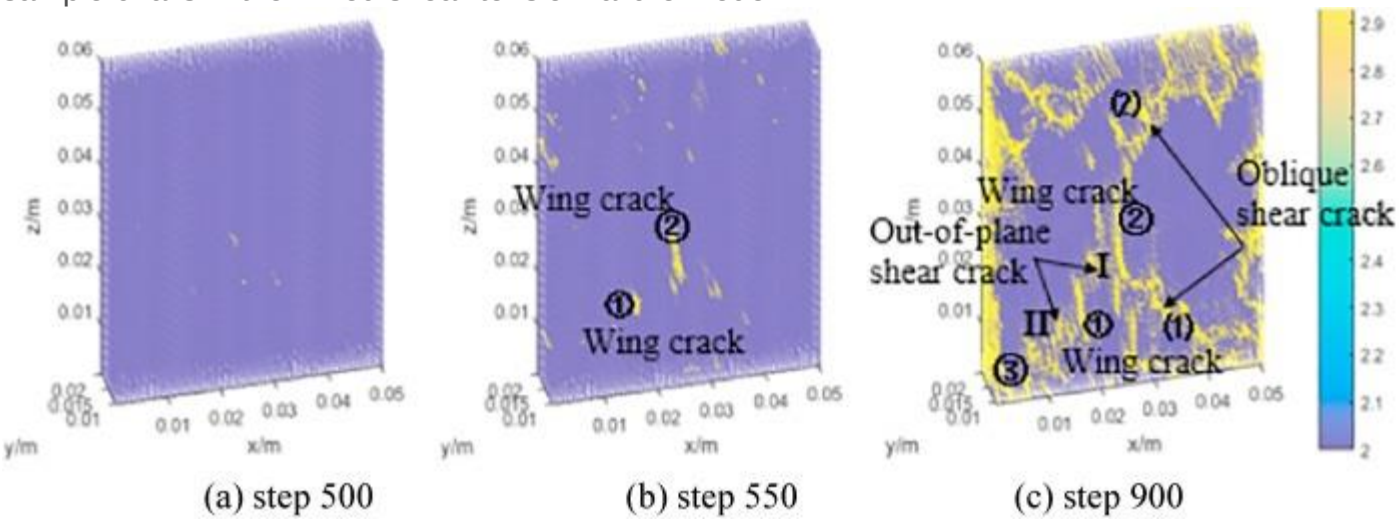

1. Download high-res image (268KB)
2. Download full-size image

Fig. 21. Crack initiation, propagation and coalescence in rectangular specimen at strain rate of 66.67s-1.

Compared with sample 5 and sample 4, the number of cracks and fractions of sample 6 increases obviously. Furthermore, the crack initiation stress, peak stress and peak normal strain of sample also increase obviously. The stress-strain curves obtained from GPD of sample 6 is plotted in Fig. 22. The crack initiation stress increases from

78.26 MPa in sample 4 to 125.32 MPa in sample 6. The peak stress of sample increases from 92.01 MPa in sample 4 to 134.30 MPa in sample 6. The peak strain in sample 4 is 0.271%. However, the peak strain is 0.331% in sample 6. That is to say, the crack initiation stress and the peak stress increase with increasing strain rate.

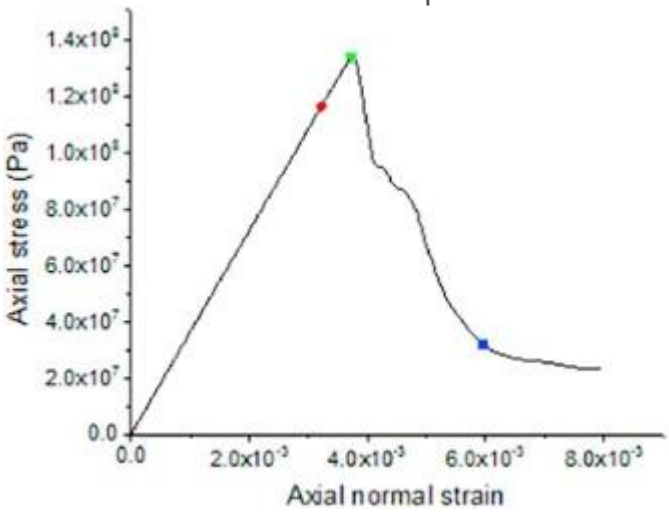

1. Download high-res image (42KB)
2. Download full-size image

Fig. 22. Stress-strain curves obtained from GPD of sample 6 at strain rate of 66.67/s.

Four stress-strain curves of samples with heterogeneity coefficient $w = 20$ are plotted in Fig. 23. The strain rate has a significant influence on the strength of rock samples. And stress-strain curves show the brittle characteristics because the elastic-brittle constitutive model is applied in this paper. Moreover, the uniaxial dynamic compressive strength and the peak strain increase obviously with increasing strain rate. While, the Young's modulus increases slightly with increasing strain rate, as shown in Fig. 23.

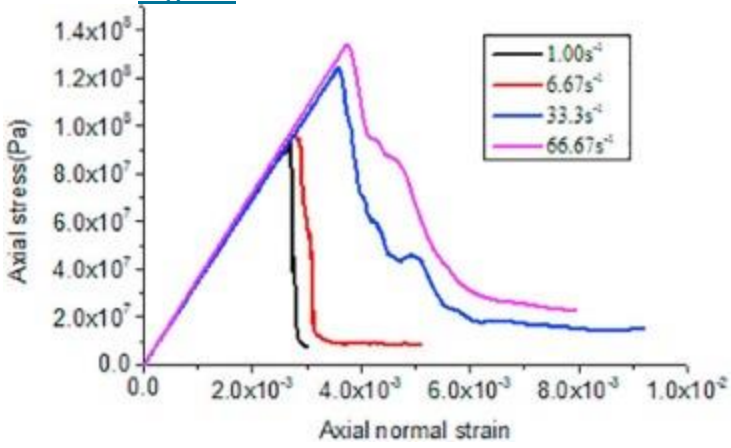

1. Download high-res image (65KB)
2. Download full-size image

Fig. 23. Compressive axial stress versus axial strain at the different strain rate from 1.0 s^{-1} to 66.67 s^{-1}.

3.3.3. High strain rate

In this subsection, five typical strain rates are chosen to study the mechanical characteristics and the failure mode of rectangular rock specimens under high speed impact compression. The strain rate can be defined as $\dot{\varepsilon}=\frac{Loading velocity}{Sample height}=\frac{v}{0.06}$. The different strain rates versus different loading speeds are listed in Table 3.

Table 3. The relationship between loading speed and strain rate.

Loading speed	8 m/s	10 m/s	20 m/s	30 m/s	40 m/s
Strain rate	133.33 s^{-1}	166.67 s^{-1}	333.33 s^{-1}	500 s^{-1}	666.67 s^{-1}

The strain rates in this subsection belong to the range of high strain rate based on strain rate determination method because the strain rate is larger than 10^2 s^{-1}. In this subsection, the heterogeneity coefficient $w = 20$ is considered due to the limited space of this paper.

3.3.3.1. The strain rate of 133.33 s^{-1}

This model is defined as the sample 7. As shown in Fig. 24, when the loading reaches step 200, the compression stress reaches 103.03 MPa, wing crack ① first initiates from the middle of sample. When the loading reaches step 282, the compression stress reaches peak value of 145.77 MPa, wing crack ② initiates from the middle of the sample and propagate towards the top and bottom edges of the sample 7. After peak stress, the stress decreases sharply. When the loading reaches step 400, the compression stress drops to 44.86 MPa, wing cracks ① and ② continue to propagate towards the top and bottom edges. At the same time, oblique shear crack (1) coalesces with wing crack ②. When the loading reaches step 1000, the compression stress drops to 26.47 MPa. Oblique shear crack (2) coalesces with wing crack ②; oblique shear crack (3) coalesces with wing crack ①. Finally, the sample 7 fails in the mixed shear-tension failure mode. Moreover, the sample 7 is broken into 10 fragments.

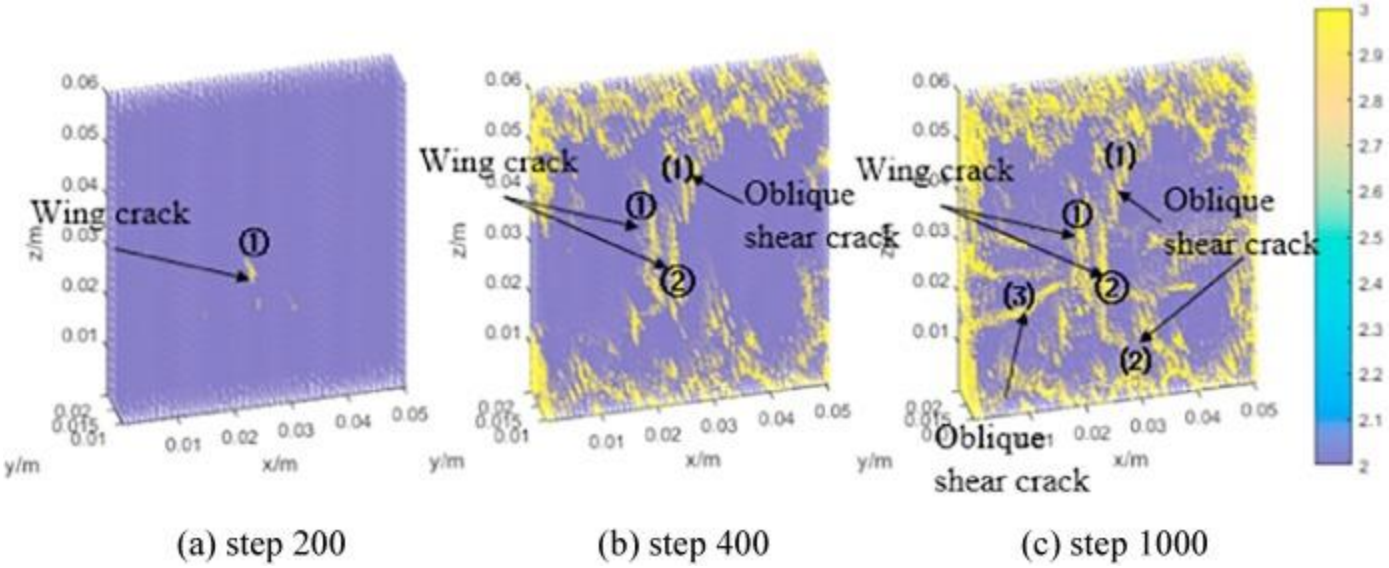

1. Download high-res image (337KB)
2. Download full-size image

Fig. 24. Crack initiation, propagation and coalescence in rectangular sample 7 at strain rate of 133.33 s^{-1}.

3.3.3.2. The strain rate of 166.67 s^{-1}

In the sample 8, the strain rate increases to 166.67 s^{-1}. As shown in Fig. 25, at loading step200, the compression stress is 143.57 MPa, a horizontal shear zone first initiates from the middle of sample. When the loading reaches step 226, the compression stress reaches the peak value of 173.13 MPa. When the loading reaches step 500, the compression stress drops to 75.02 MPa, oblique shear crack (1) coalesces with oblique shear crack (2), oblique shear crack (3) coalesces with oblique shear crack (4). When the loading reaches step 2000, the compression stress drops to 53.61 MPa, the failure of the sample 8 occurs. In addition, the sample 8 is broken into 12 fragments.

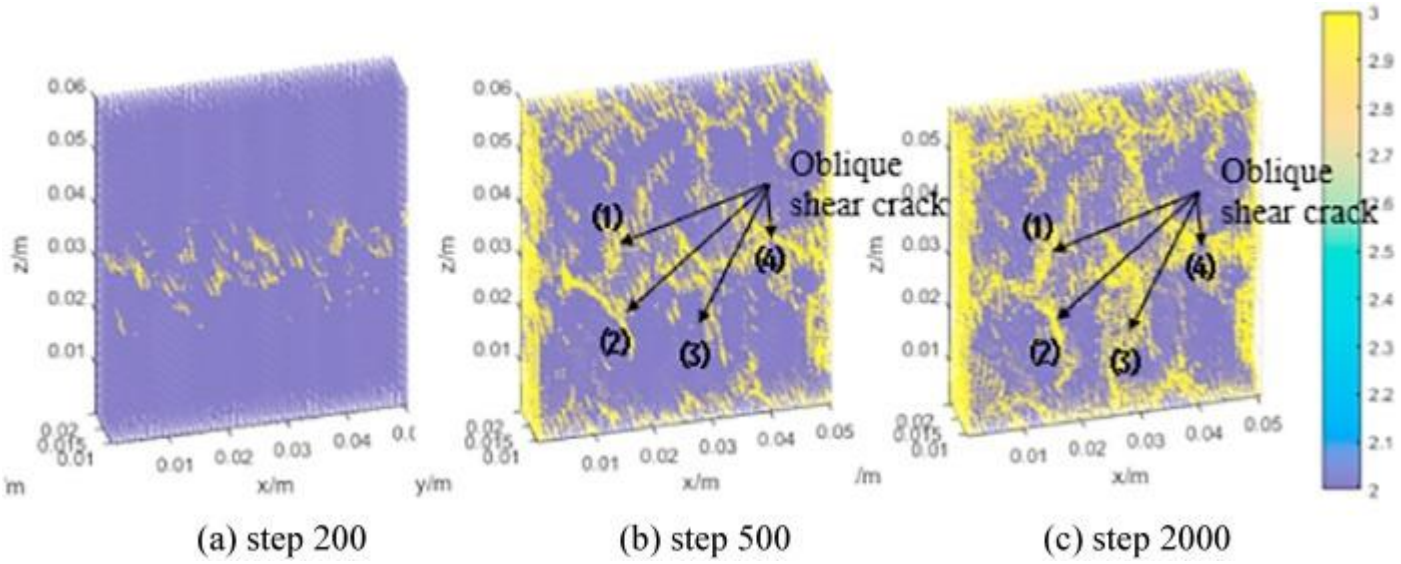

1. Download high-res image (344KB)
2. Download full-size image

Fig. 25. Crack initiation, propagation and coalescence in rectangular sample 8 at strain rate of 166.67 s^{-1}.

3.3.3.3. The strain rate of 333.33 s^{-1}

In the sample 9, the strain rate increases to 333.33 s^{-1}. As shown in Fig. 26, when loading reaches step 50, the compression stress is 65.74 MPa, cracks initiate from the top and bottom edges of the sample 9. When loading reaches 134 step, the compression stress reaches the peak value of 175.79 MPa. When the loading reaches step 150, a horizontal shear zone emanates in the middle of the sample 9. At the same time, wing cracks (①, ② and ③) are initiated from the horizontal shear zone and propagate along the direction of the maximum principal stress. When the loading reaches step 850, wing crack ① initiating from the middle of sample propagates through the whole sample, oblique shear crack (1) initiating from the bottom edge of sample coalesces with wing crack ②, oblique shear crack (2) coalesces with the horizontal shear zone. Finally, the sample 9 fails in the mixed shear-tension failure mode. In addition, the sample 9 is broken into 10 fragments.

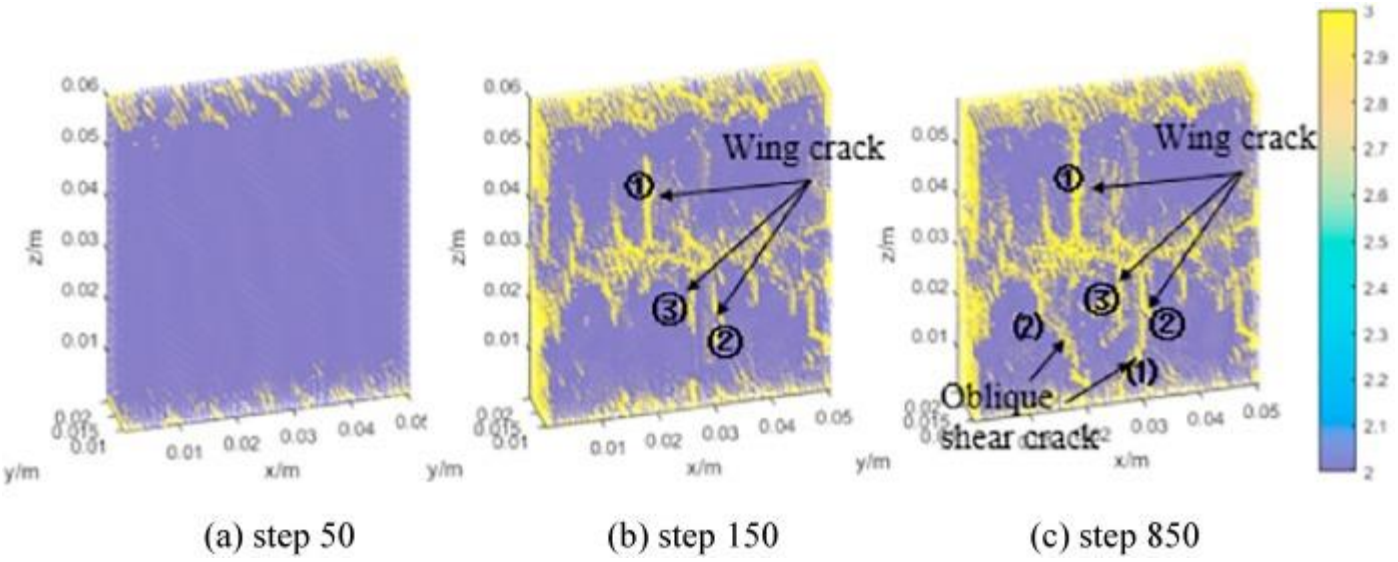

1. Download high-res image (311KB)
2. Download full-size image

Fig. 26. Crack initiation, propagation and coalescence in rectangular sample 9 at strain rate of 333.33 s^{-1}.

3.3.3.4. The strain rate of 500 s^{-1}

In the sample 10, the strain rate increases to 500 s^{-1}. As shown in Fig. 27, when loading reaches step 40, the compression stress is 80.32 MPa, wing cracks first initiate from the top and bottom edges of sample 10, which is different from the sample 9. When the loading reaches step 86, the compression stress reaches peak value of 180.72 MPa. After peak stress, the stress decreases sharply. When the loading reaches step 100, wing cracks ①, ②, ③ and ④ propagate along the direction of the maximum principal stress, oblique shear cracks (1) and (2) coalesce with each other. When the loading reaches step 650, wing crack ① coalesces with oblique shear crack (3), wing crack ② coalesces with oblique shear crack (4), wing crack ③ coalesces with oblique shear crack (5). Finally, the sample fails in the mixed mode of shear-tension failure mode. In addition, the sample 10 is broken into 13 fragments.

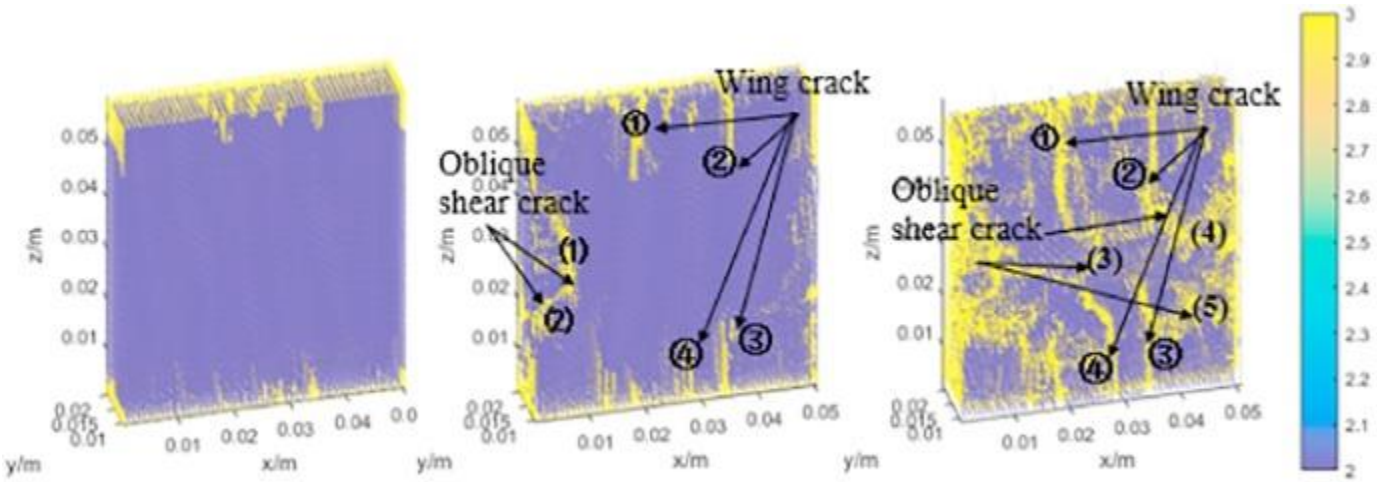

(a) step 40 (b) step 100 (c) step 650

1. Download high-res image (307KB)
2. Download full-size image

Fig. 27. Crack initiation, propagation and coalescence in rectangular sample 10 at strain rate of 500 s^{-1}.

3.3.3.5. The strain rate of 666.67 s^{-1}

In the sample 11, the strain rate increases to 666.67 s^{-1}. The failure mode of the sample 11 is similar to that of the sample 10 at the strain rate of 500 s^{-1}. When loading reaches step 40, the compression loading is 108.23 MPa, wing cracks initiate from the loading edge firstly. When the loading reaches step 74, the compression stress reaches peak value of 189.42 MPa. After peak stress, the stress decreases sharply. When the loading reaches step 110, wing cracks ①, ②, ③, ④ and ⑤ propagate along the loading direction. Oblique shear crack (1) coalesces with the wing cracks ① and ②. Oblique shear crack (2) coalesces with wing crack ⑤. Oblique shear crack (3) coalesces with wing crack ④. When the loading step reaches 700, wing crack ② coalesces with wing crack ③, oblique crack (4) coalesces with wing cracks initiating from the bottom edge of sample. Finally, the sample 11 fails in the mixed mode of shear-tension failure mode. In addition, the sample 11 is broken into 20 fragments (see Fig. 28).

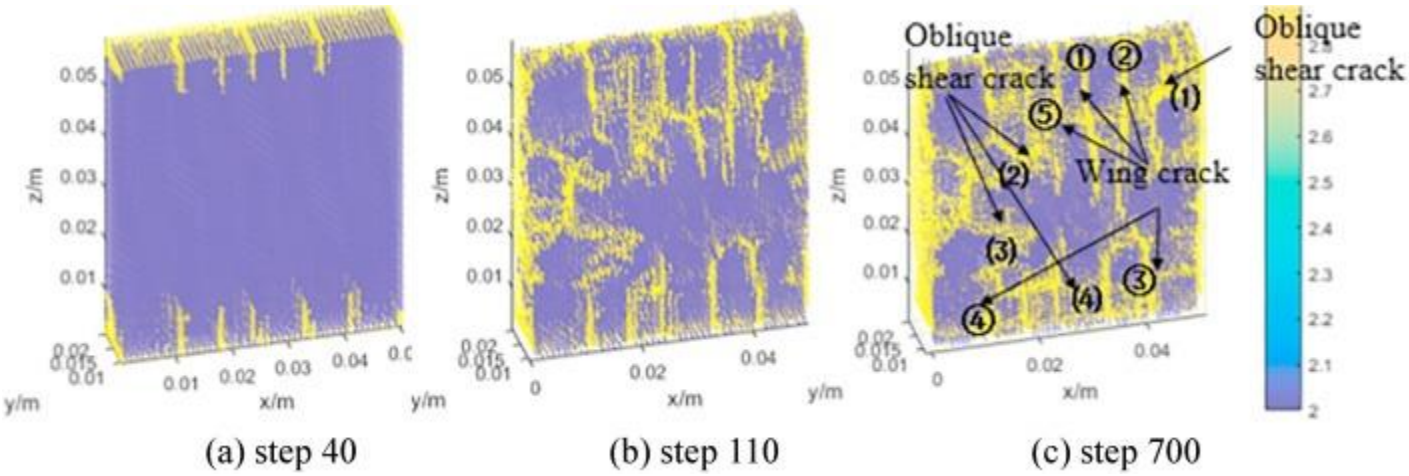

1. Download high-res image (330KB)
2. Download full-size image

Fig. 28. Crack initiation, propagation and coalescence in rectangular sample 11 at strain rate of666.67 s^{-1}.

3.4. The effect of strain rate on the strength

The ratio of dynamic strength or dynamic fracture toughness to static strength is always studied. This ratio, which is expressed by logarithmic function of loading rate, is generally defined as dynamic increase factor or normalized dynamic strength (σd/σs). Based on the previous works, the peak strength of samples hardly depends on loading speed when it is less than 0.06 m/s [46]. Therefore, in this paper, loading speed of 0.06 m/s is considered as the quasi-static condition. Table 4 shows the peak strength at different strain rate.

Table 4. Peak strength at different strain rate.

Loading speed, i.e. strain rate $\dot{\varepsilon}$	Peak strength (MPa)	Dynamic Increase Factors (DIF)
0.06 m/s, i.e. 1.000 s^{-1}	92.11	1.000
0.4 m/s, i.e. 6.667 s^{-1}	96.44	1.047
2 m/s, i.e. 33.333 s^{-1}	123.93	1.345
4 m/s, i.e. 66.667 s^{-1}	134.30	1.458
8 m/s, i.e. 133.333 s^{-1}	145.77	1.583
10 m/s, i.e. 166.667 s^{-1}	173.13	1.784
20 m/s, i.e. 333.3331 s^{-1}	175.79	1.908
30 m/s, i.e. 500.000 s^{-1}	180.72	1.962
40 m/s, i.e. 666.667 s^{-1}	189.42	2.056

Grady and Lipkin [47] summarized a wide applied experience formula of dynamic uniaxial compressive strength of rocks as:

(8)$\sigma_{ucd}=a\dot{\varepsilon}^{n}$

where $\dot{\varepsilon}$ is between 10^{0} and 10^{5}/s, n is less than 1/3.

Then, the fitting curve of dynamic uniaxial compressive strength and strain rate in Table 4 is plotted in Fig. 29. It has been found from Fig. 29 that the dynamic increment factor increases with an increase in the strain rate.

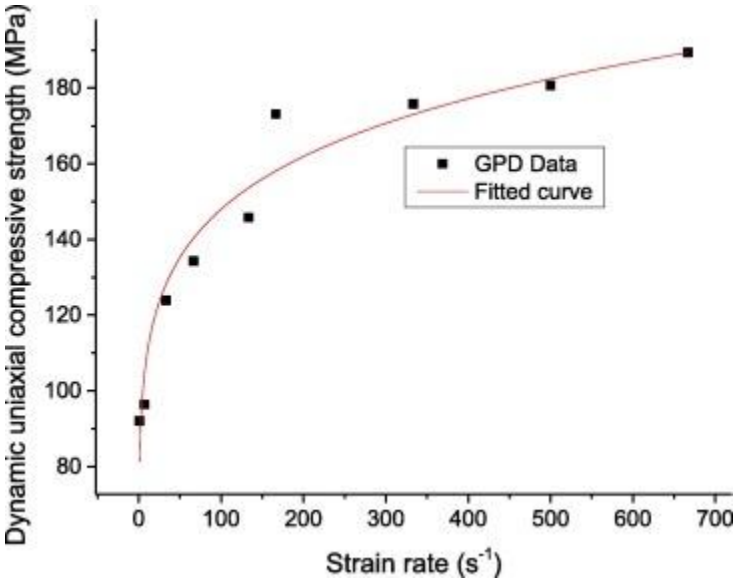

1. Download high-res image (122KB)
2. Download full-size image

Fig. 29. Fitting curve of dynamic uniaxial compressive strength vs strain rate.

As shown in Fig. 29, the relation between dynamic uniaxial compressive strength and strain rate can be obtained as:

(9)$\sigma_{ucd}=8.688\times\dot{\varepsilon}^{0.117}$

In order to discuss the difference between dynamic increment factor obtained from GPD and experiments, the relation between dynamic increment factor and strain rate $\dot{\varepsilon}$ varying from 1.000 s^{-1} to 166.667 s^{-1} is plotted in Fig. 30. The variation law of dynamic increment factor in GPD is in good agreement with that by Ma et al. [48], as shown in Fig. 30. When the strain rate is close to 133.33 s^{-1}, the increase of dynamic increment factor is sharp. This critical value is similar to that of limestone obtained in experiment [49].

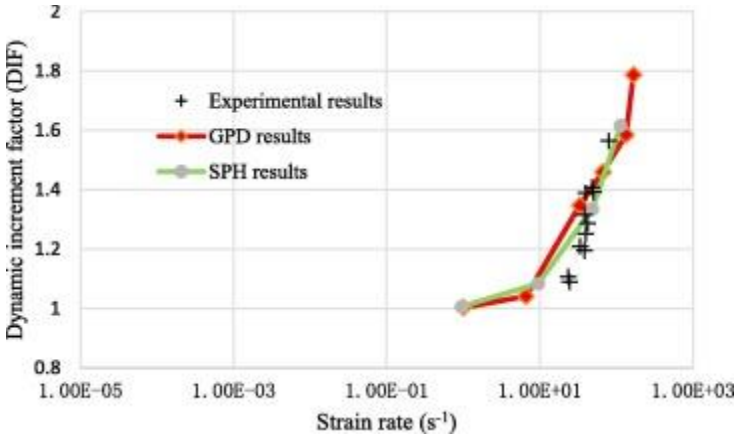

1. Download high-res image (116KB)
2. Download full-size image

Fig. 30. Relationship between dynamic increment factor and strain rate.

3.5. The effect of strain rate on the number of fractions

As mentioned above, failure mode of samples transforms from tensile mode to the mixed shear-tension mode with increasing loading speed. The loading speed of 2 m/s is the transition point. That is to say, the failure mode of samples is the mixed shear-tension one when the loading speed is more than 2 m/s, while the failure mode of samples is tensile one when the loading speed is less than 2 m/s. Meanwhile, the number of broken blocks of samples increases with increasing loading speed, and the size of broken blocks decreases with increasing loading speed. For example, the number of fractions reaches 2 when the loading speed is equal to 0.06 m/s, while the number of fractions is equal to 20 when the loading speed reaches 40 m/s, as shown in Fig. 31. This results are also in good agreement with other works [49].

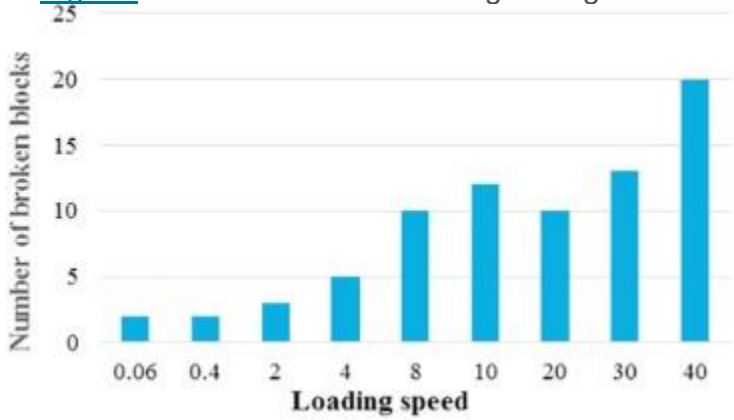

1. Download high-res image (30KB)
2. Download full-size image

Fig. 31. Bar chart of the number of broken blocks.

4. Conclusions

The General Particle Dynamics code (GPD) is developed to simulate initiation, propagation and coalescence of cracks in 3D non-homogeneous rock-like materials subjected to dynamic loads. The elasto-brittle damage model is applied to reflect the initiation and growth of cracks and the macro-failure of the rock-like materials. The numerical results of pre-notched semi-circular bend show that GPD is capable of realistically simulating the mechanical behavior of rock materials subjected to dynamic loads.

Under high strain rate, the fracture modes of rock samples are no longer a single vertical crack of transfixion damage, but many cracks propagate at the same time. When the loading speed increases, the number of vertical cracks increases, the horizontal crack propagation speed increases, the number of broken blocks of samples increases, and the size of broken blocks decreases, which are in good agreement with experiments.

The uniaxial dynamic compressive strength and the peak strain increase obviously with increasing loading speed. The numerical results show that relationship between dynamic uniaxial compressive strength and strain rate obtained from GPD is consistent with the empirical formula. However, the Young's modulus increases slightly with increasing loading speed.

In addition, the failure mode of samples transform from splitting failure to the mixed shear-tension failure with decreasing heterogeneity coefficient. Moreover, the number of cracks and fractions increases with decreasing heterogeneity coefficient.